JOURNAL OF THE AMERICAN CHEMICAL SOCIETY

Subscriber access provided by Temple University Libraries

Article

Excited State Dynamics of a CsPbBr3 Nanocrystal Terminated with Binary Ligands: Sparse Density of States with Giant Spin-Orbit Coupling Suppresses Carrier Cooling

Aaron Forde, Talgat M Inerbaev, Erik K. Hobbie, and Dmitri S. Kilin

J. Am. Chem. Soc., **Just Accepted Manuscript** • DOI: 10.1021/jacs.8b13385 • Publication Date (Web): 04 Feb 2019

Downloaded from http://pubs.acs.org on February 4, 2019

Just Accepted

“Just Accepted” manuscripts have been peer-reviewed and accepted for publication. They are posted online prior to technical editing, formatting for publication and author proofing. The American Chemical Society provides “Just Accepted” as a service to the research community to expedite the dissemination of scientific material as soon as possible after acceptance. “Just Accepted” manuscripts appear in full in PDF format accompanied by an HTML abstract. “Just Accepted” manuscripts have been fully peer reviewed, but should not be considered the official version of record. They are citable by the Digital Object Identifier (DOI®). “Just Accepted” is an optional service offered to authors. Therefore, the “Just Accepted” Web site may not include all articles that will be published in the journal. After a manuscript is technically edited and formatted, it will be removed from the “Just Accepted” Web site and published as an ASAP article. Note that technical editing may introduce minor changes to the manuscript text and/or graphics which could affect content, and all legal disclaimers and ethical guidelines that apply to the journal pertain. ACS cannot be held responsible for errors or consequences arising from the use of information contained in these “Just Accepted” manuscripts.

ACS Publications

is published by the American Chemical Society. 1155 Sixteenth Street N.W., Washington, DC 20036

Published by American Chemical Society. Copyright © American Chemical Society. However, no copyright claim is made to original U.S. Government works, or works produced by employees of any Commonwealth realm Crown government in the course of their duties.

Excited State Dynamics of a $CsPbBr_3$ Nanocrystal Terminated with Binary Ligands: Sparse Density of States with Giant Spin-Orbit Coupling Suppresses Carrier Cooling

Aaron Forde,[1] Talgat Inerbaev,[2,3,4] Erik Hobbie,[1] Dmitri S. Kilin[5]*

[1] *Department of Materials Science and Nanotechnology, North Dakota State University, Fargo, North Dakota 58102, United States*

[2] *Sobolev Institute of Geology and Mineralogy SB RAS, Novosibirsk*

[3]*National University of Science and Technology MISIS, 4 Leninskiy pr., Moscow 119049, Russian Federation*

[4] *L. N. Gumilyov Eurasian National University, Astana, Kazakhstan*

[5]*Department of Chemistry and Biochemistry, North Dakota State University, Fargo, North Dakota 58102, United States*

*Corresponding Author: dmitri.kilin@ndsu.edu

ABSTRACT

Fully inorganic lead halide perovskite nanocrystals (NCs) are of interest for photovoltaic and light emitting devices due to optoelectronic properties that can be tuned/optimized via halide composition, surface passivation, doping, and confinement. Compared to bulk materials, certain excited-state properties in NCs can be adjusted due to electronic confinement effects such as suppressed hot carrier cooling and enhanced radiative recombination. Here we use spinor Kohn-Sham orbitals (SKSOs) with spin-orbit coupling (SOC) interaction as a basis to compute excited-state dissipative dynamics simulations on a fully-passivated $CsPbBr_3$ NC atomistic model. Redfield theory in density matrix formalism is used to describe electron-phonon interactions which drive hot carrier cooling and non-radiative recombination ($k_{non-rad}$). Radiative recombination (k_{rad}) is calculated through oscillator strengths using SKSO basis. From k_{rad} and $k_{rad} + k_{non-rad}$ we compute a theoretical photoluminescence quantum yield (PLQY) of 53%. Computed rates of hot carrier cooling ($k_{cooling} \sim 10^{-1}$ $1/\mathrm{ps}$) compare favorably with what has been reported in the literature. Interestingly, we observe that hot electron cooling slows down near the band edge, which we attribute to large SOC in the conduction band combined with strong confinement, which create sub-gaps above the band edge. This slow carrier cooling could potentially impact hot carrier extraction before complete thermalization in photovoltaics (PVs). Implications of this work suggest that strong/intermediate confined $APbX_3$ NCs are better suited towards applications in PVs, due to slower carrier cooling near the conduction band edge, while intermediate/weak confined NCs are more appropriate for light emitting applications, such as LEDs.

Introduction

$APbX_3$ (A=Cs,methylammonium(MA), formadamidinium (FA): X=I, Br, Cl) lead halide perovskite nanocrystals[1] (NCs) have become popular materials for a variety of technology applications due to their facile wet-chemical synthesis, tunable chemical composition, and size-dependent photo-physical properties. The 'phase space' of possible chemical compositions – regimes of electronic confinement, surface termination, and doping – allow for engineering and optimizing electronic excited-state processes for device applications. In semiconducting nanocrystals, the primary excited-state processes of interest for devices are: hot carrier cooling, charge carrier recombination, and carrier multiplication which is also known as multi-exciton generation (MEG). For photovoltaics, slow hot carrier cooling, long charge carrier lifetimes, and MEG are needed to maximize power conversion efficiency.[2] For light-emitting applications, such as lasing and LEDs, fast hot carrier cooling with fast radiative recombination and slow non-radiative recombination is needed to maximize external quantum efficiencies.

Experimental and computational studies have shown correlations between rates of excited state processes and the chemical composition/physical structure of $APbX_3$ perovskites. Halide anion composition has been shown to have significant effects on non-radiative recombination rates, with iodides providing slower rates than bromine based perovskites.[3] Cation composition has been shown to have an impact on hot carrier cooling and non-radiative recombination rates, with organic cations providing faster rates than inorganic Cs^+ ions.[4-5] It is also expected that organic cations promote polaron formation which would screen phonons, reducing cooling and nonradiative recombination.[6-8] The role of confinement on hot carrier cooling indicates that at low excitation densities (~10^{17} cm^{-1}) strong confinement slows down carrier cooling in $MAPbBr_3$ and $FAPbI_3$ NCs,[9,10] while at high excitation densities (~10^{19} cm^{-1}) the trend reverses and rates of cooling for strongly confined NCs become slower compared to less confined NCs. Efficient MEG has been observed in confined $FAPbI_3$ NCs[10] which has been supported by computer simulations. [11] Theory predicts that radiative recombination rates show a strong dependence on quantization, with weak/intermediately confined NCs showing faster rates compared to strongly confined NCs because of bright triplet excitons.[12]

A common feature that all of the above mentioned $APbX_3$ materials have is that their valence band is composed of hybridized *X-np* (n=principle quantum number) and *Pb-6s* orbitals while the conduction band is comprised of hybridized *Pb-6p* orbitals which experience a large spin-orbit coupling (SOC). Theory and calculations have shown that this type of electronic structure is beneficial for high defect tolerance.[13-14] but its role on excited state dynamics has been relatively unexplored. On one hand, it would be expected that SOC would increase rates of carrier cooling due to the relaxation of spin selection rules for non-adiabatic coupling (NAC). On the other hand, the SOC interaction results in the J=1/2 angular momentum state being spilt from the J=3/2 state and reduces the bandgap by ~0.70 eV.[15-16] One expectation is that such a large energy splitting would make the density of states (DOS) near the conduction band edge sparse. Combined with the quantization of bands that occurs in strongly confined NCs, it would seem possible that sub-gaps appear near the band edges of $APbX_3$ NCs and cause a 'phonon bottleneck'. In bulk $MAPbI_3$ it has been reported that SOC accelerates carrier cooling due to enhanced electronic coupling,[17] but the role of confinement on carrier cooling has not been investigated to date.

The *'phonon bottleneck'* has been a predicted feature of confined nanostructures and is expected to be observed when there is a lack of phonon modes in resonance with electronic sub-gaps giving rise to extended hot-carrier lifetimes.[18] Strongly confined NCs/QDs appeared to be the model material to observe the bottleneck effect due the energy spectrum being discrete, but the effect has been elusive to observe in experiment at low excitation densities. At high excitation densities where the average number of photo-excited particles $\langle N \rangle > 1$ the effect has been observed for $APbX_3$ perovskite NCs[19] and thin-films.[20-21,22]

Here we report the observation of a 'phonon bottleneck' in our *ab initio* excited-state electron dynamics simulation of a $CsPbBr_3$ NC fully-passivated with short chain organic ligands where $\langle N \rangle = 1$. Our excited-state dynamics couple electronic and nuclear degrees of freedom through NACs allowing hot carriers to dissipate energy as phonons. With strong confinement and strong SOC in the conduction band, large electronic sub-gaps appear which slow down hot-electron cooling. We also compare rates of non-radiative recombination to radiative recombination rate to compute a PLQY=53%. Along the way we describe ground state electronic structure and absorption spectra and compare features of computed spectra to experimentally measured spectra to colloidal ensemble of $CsPbBr_3$ NCs.

Methods

Construction of the fully-passivated $CsPbBr_3$ atomistic model follows experimental observations regarding surface termination. Elemental analysis studies have shown that with decreased NC size the surface shows a greater proportion of RNH_3^+ termination.[23] This would require that the carboxyl group protonate the amine which has been shown to occur in these systems.[24] So, in a sense the protonated amine and deprotonated carboxyl are correlated with one another. What is most likely is that the surface is partially terminated by both Pb-Br and Pb-$RCOO^-$, due to the stoichiometry of the surface. Another motivation for termination with $RCOO^-$ is to provide the NC with a non-vacuum dielectric layer which would compare better to experimental settings. Thus, we took the bulk $CsPbBr_3$ crystal structure, carved out a 2x2x2 unit cell, and coordinated acetate/ethylammonium ions to surface atoms Pb^{2+}/ Br^-.

Overall, this gives a structure of $Cs_8Pb_{27}Br_{54}$ passivated with 54/48 acetate/ethylammonium ligands for a total of 995 atoms and 2808 electrons. The atomistic model is shown in **Figure 1(a).** This composition gives a NC that has an edge length of ~1.5 nm. With the model NC being smaller than those in experiment, it is likely that some features from our calculations are not literal reflections of the electronic structure for larger NCs. With a larger surface to volume ratio, it is likely that surface distortions reduce the symmetry of the wavefunctions. Further structural details (bond distances, bond angles, radial distribution functions) can be found in the *Supporting Information* (SI) **Figures S1 -S3** and SI **Table S1**.

The ground state electronic structure of our atomistic model was found using DFT with the generalized gradient approximation (GGA) Perdew-Burke-Ernzerhof (PBE) functional[25] in a plane-wave basis set along with projector augmented-wave (PAW) pseudopotentials[26-27] in VASP[28] software. All calculations were performed at the gamma point. A simulation cell size of 31x31x31 Å with 7 Å of vacuum in each direction was used to minimize interaction across a periodic boundary.

Here we describe the methodology used to compute observables which have been documented elsewhere[29,30] and with extended details in the SI. We use non-collinear spin (NCS) DFT and include relativistic contributions to the Kohn-Sham (KS) Hamiltonian. Within VASP, relativistic effects are treated perturbatively as scalar corrections which include the spin-orbit interaction $L \cdot S$. Solutions to the relativistic KS Hamiltonian generate two-component spinor KS orbitals (SKSOs) $\varphi_i^{SKSO}(\vec{r}) = \begin{Bmatrix} \varphi_{i\alpha}(\vec{r}) \\ \varphi_{i\beta}(\vec{r}) \end{Bmatrix}$. SKSOs can be interpreted to be a superpositions of α and β spin projections. These SKSOs are implemented as the basis to compute ground state properties and excited state dynamics.

To compute absorption spectra, we work under the independent orbital approximation (IOA) where excited-states are described as a pair of orbitals, as opposed to a superposition of orbitals commonly used in TDDFT or Bethe-Salpeter approaches. Optical transitions between SKSO *i* and *j* can be found through transition dipole matrix elements $\langle \vec{D}_{ij} \rangle = -e \int d\vec{r} \{ \varphi_{i\alpha}^{*} \quad \varphi_{i\beta}^{*} \} \vec{r} \begin{Bmatrix} \varphi_{j\alpha} \\ \varphi_{j\beta} \end{Bmatrix}$ to determine oscillator strengths $f_{ij} = \left| \vec{D}_{ij} \right|^{2} \frac{4\pi m_e v_{ij}}{3\hbar e^2}$. With known oscillator strengths, an absorption spectrum can be computed through $\alpha^{SKSO}(\varepsilon) = \sum_{ij} f_{ij} \delta(\varepsilon - \Delta\varepsilon_{ij})$ where the delta function is approximated as a Gaussian to provide thermal broadening.

A description of excited-state dissipative dynamics, such as hot carrier cooling and non-radiative recombination, requires using techniques that go beyond the Born-Oppenheimer approximation to couple electronic and nuclear degrees of freedom. We do this by computing NACs V_{ij} which describe the probability of occupation transitions between two potential energy surfaces. Two common approaches are used to compute NACs: (1) along normal mode (ζ_I) coordinates [31-32] $V_{ij} = \left\langle \varphi_i^{SKSO}(\vec{r};R(t)) \left| \frac{d}{d\zeta_I} \right| \varphi_j^{SKSO}(\vec{r};R(t)) \right\rangle \frac{d\zeta_I}{dt}$ and (2) in an 'on-the-fly'[33] fashion as $V_{ij} = \left\langle \varphi_i^{SKSO}(\vec{r};R(t)) \left| \frac{d}{dt} \right| \varphi_j^{SKSO}(\vec{r};R(t)) \right\rangle$. $R(t) = \{ \vec{R}_I(t) \}$ represents displacement of ions *I* due to thermal motion with $\varphi_j^{SKSO}(\vec{r};R(t))$ being an adiabatic state that depends parametrically on $R(t)$. Here we use adiabatic molecular dynamics (MD) to compute NACs 'on-the-fly' along a MD trajectory as

$$\hat{V}_{ij}^{NA}(t) = -\frac{i\hbar}{2\Delta t} \int d\vec{r} \left\{ \varphi_{i\alpha}^{*}(\vec{r},\{\vec{R}_I(t)\}) \quad \varphi_{i\beta}^{*}(\vec{r},\{\vec{R}_I(t)\}) \right\} \cdot \begin{Bmatrix} \varphi_{j\alpha}(\vec{r},\{\vec{R}_I(t+\Delta t)\}) \\ \varphi_{j\beta}(\vec{r},\{\vec{R}_I(t+\Delta t)\}) \end{Bmatrix} + h.c. \qquad (1)$$

where $\Delta t = 1fs$ represents the timestep in the MD trajectory. We note that each spinor component contributes to the NAC matrix element.

The time evolution of electronic degrees of freedom that are weakly coupled to a thermal bath can be described using the Redfield quantum master equation [34,35] in the density matrix formalism;

$$\frac{d}{dt}\hat{\rho} = -\frac{i}{\hbar}\sum_k (F_{ik}\rho_{kj} - \rho_{ik}F_{kj}) + \left(\frac{d\rho_{ij}}{dt}\right)_{diss} \quad (2)$$

where F is the many-electron Fock matrix and ρ is the density matrix. The first term is the Liouville – von Neumann equation describing the unitary time evolution of a closed system while the second term describes electronic energy dissipation due to weak coupling to a thermal bath. Dissipative transitions are treated perturbatively to 2nd order with respect to electron-phonon interaction and can be interpreted as state-to-state transitions analogous to Fermi's Golden Rule. To generate dissipative state-to-state transition rates, autocorrelation of NACs and a subsequent Fourier transform provides average time-independent transition rates, referred to as components of the Redfield tensor. Components of the Redfield tensor control the dissipative dynamics of the density matrix $\left(\frac{d\rho_{ij}}{dt}\right)_{diss} = \sum_{lm} R_{ijlm}\rho_{lm}$.

Initial conditions for excited state dynamics are chosen based on oscillator strengths for most intense optical transitions with transition energy $\hbar\Omega_{ij} = E^{tot}_{i\to j} - E^{tot}_{ground} \approx \varepsilon_j - \varepsilon_i$. Along the trajectory, we compute time-resolved observables, such as changes in charge carrier occupation $n^{(a,b)}$ $(\varepsilon,t) = \sum_i \rho^{(a,b)}_{ii}(t)\delta(\varepsilon - \varepsilon_i)$ =, where $\rho^{(a,b)}_{ii}(t)$ represent time evolving occupations of states in the conduction/valence band and average charge carrier energy $\langle\Delta\varepsilon_{e/h}\rangle(t) = \sum_{i \geq LU/HO \geq i} \rho_{ii}(t)\varepsilon_i(t)$. To get rates of charge carrier relaxation to band edges, we convert energy expectation value into a dimensionless energy and fit energy relaxation to a single exponential decay to solve for the rate constant, $k_e = \{\tau^e\}^{-1} = \left\{\int_0^\infty \langle E_e \rangle(t) dt\right\}^{-1}$.

The efficiency of PL from our atomistic model is PLQY $= \frac{k_{rad}}{k_{rad} + k_{non-rad}}$, where $k_{non-rad}$ is determined from the Redfield tensor components corresponding to the lowest energy transitions across the bandgap. The radiative rate constants k_{rad} are found from Einstein coefficients for spontaneous emission of optical transitions across the bandgap[36]; $A_{ij} = \frac{8\pi^2 v_{ij}^2 e^2}{\varepsilon_0 m_e c^3} \frac{g_i}{g_j} f_{ij}$ where v_{ij} represents transition frequency between states, f_{ij} represents the oscillator strength, or probability, of transition between states, g_i and g_j represent the degeneracy of electronic state i and j, and the other symbols represent the familiar fundamental constants.

Results - Ground State Properties.

SKSO DOS for the geometry optimized NC is shown in **Figure 1(b)** and is computed as $D_{SKSO} = \sum_i \delta\left(\varepsilon - \varepsilon_i^{SKSO}\right)$ with the delta function being approximated as a Gaussian distribution. Shaded regions represent occupied states. There are four relevant observations about the DOS. First, there is a 'clean' bandgap indicating the NC is properly passivated with no trap states.[37] Second, the band gap has a value of 2.40 eV (521 nm). Third, each eigenenergy is twice degenerate which follows experiment[38] and theory[12] with degenerate bands having antiparallel magnetization vectors. Lastly, the DOS peaks near the band edges show a trend analogous to particle in a box envelope functions which we label with symmetry indices s_x, p_x, and d_x *(x=e,h)*, respectively.

Prior to analysis of optical properties in **Figure1(c)** we focus on the pDOS calculations, see **Figure 1(d)**, show the atomic orbital composition of the conduction and valence band. In the valence band, it is seen that the s_h', p_h', and d_h' states have the same atomic orbital composition of Br-4p (red, dotted-space-dotted), Pb-6s (green, dot dash), and O-2p (pink, dashed), but in different proportions. States deeper in the valence band have a greater proportion of Br-4p contribution to the DOS. For the bottom of the conduction band, the s_e, p_e, and d_e states have essentially the same proportion of Pb-6p (blue, dot-dash-dash-dot) states and experience little hybridization with ligand states. An interesting note is that within 1.5 eV of the conduction and valence band edge, there was no hybridization of the protonated amine ligands with the NC and only the O-2p states of the deprotonated carboxylic acid contribute electron density for chemical bonding.

From the ground state electronic structure, we compute optical spectra, **Figure 1(c),** of the NC from under IOA. Within **Figure 1(c)** we plot computed absorption spectrum (red, solid), EDOS (green, dash dot), and experimental spectra of $CsPbBr_3$ NCs with mean size ~10nm (black, dashed). Alphabetical labels, ascending order in energy/descending in wavelength, correspond to characteristic peaks in the computed and experimental spectrum which will be discussed throughout the text. In **Table 1** we show the ten most intense optical transitions with corresponding transition energy and symmetry designation.

Physically, EDOS represents the degeneracy of optical transitions for a given energy $EDOS^{SKSO}(\varepsilon) = \sum_{ij} \delta(\varepsilon - \Delta\varepsilon_{ij})$ where $\Delta\varepsilon_{ij}$ is the transition energy. This allows to compare how spectral features are enhanced, or suppressed, by physical constraints of the system. In our case the physical constraint of the system is quantization of electronic states due to boundary conditions. Comparing EDOS to the computed absorption spectrum it is seen that the lowest energy transitions, which have low degeneracy, are weighted much larger than high energy transitions. This can be seen more explicitly using a log scale were the lowest energy transition feature ***a*** is almost 2 orders of magnitude higher than EDOS (see SI **Figure S4**). The ***b*** and ***c*** features of the computed spectra differ from EDOS by ~0.5 orders of magnitude. The experimental spectrum also shows the same trend, but with the '*b*' feature being more intense. This can be interpreted as the $s_h' \rightarrow s_e$ transitions having much larger oscillator strengths than other direct type transitions (such as $p_h' \rightarrow p_e$ and $d_h' \rightarrow d_e$) or other symmetry indirect transitions.

In comparing the computed and experimental spectra we see that, even though the atomistic model and experimental NCs differ in edge length by roughly an order of magnitude, similar characteristic peaks appear. Comparison of spectral features are shown in SI **Table S2**. The peaks **a/a'**, **c/c'**, and **d/d'** can be attributed to symmetric transitions $s_h' \rightarrow s_e$, $p_h' \rightarrow p_e$, and $d_h' \rightarrow d_e$, respectively. The major difference between the two spectra is in the 450nm to 500nm region labeled **b** and **b'**. In this region, where dipole forbidden transitions $s_h \rightarrow p_e$ and $s_e \rightarrow p_h$ are expected, absorption is more intense in the experimental spectra than in the computed spectra. This can be attributed to the fact that experimental samples have a distribution of NC sizes which will absorb with a range from approximately 450nm (large confinement regime)[1,39,23] to 510nm (intermediate confinement regime).

Results - Excited State Dynamics.

The philosophy of our excited-state dynamics calculations is illustrated in **Figure 2(a)**. We assume steady-state absorption between discrete states HO-*x* and LU+*y* with energy $h\nu$ creating photo-induced holes and photo-excited electrons. At t=0 the excitation source is removed and fully populated LU+y and HO-x states thermalize to the band-edge states LU and HO with a rates $k_{cooling}$. Once both charge carriers relax to respective HO/LU states, they can recombine though radiative or non-radiative relaxation channels with rates k_{rad} and $k_{non-rad}$. The rate constants k_{rad} and $k_{non-rad}$ determine the PLQY as $\frac{k_{rad}}{k_{rad}+k_{non-rad}}$.

To model carrier cooling, we couple electronic and nuclear degrees of freedom with adiabatic molecular dynamics and compute NACs between adiabatic states using an 'on-the-fly' procedure. Thermal fluctuations of the adiabatic KSO states are shown in SI **Figure S5.** During the adiabatic trajectory it is seen that some intermediate trap states form inside the gap but quickly disappear at subsequent timesteps. The is attributed to fluctuations in bond lengths at the NC surface. We also note that along the trajectory, none of the ligands desorb from the surface, which could be due to a liable acetate-anion ligand protonating itself from an adjacent ethylammonium cation.

Processing the NACs, using SI equations 10-11d, parameterizes the Redfield equations to provide state-to-state transitions, in the spirit of Fermi's Golden Rule. The Redfield tensor fragment for population relaxation is shown in **Figure 2(b).** The tensor is composed of states from HO-24 to LU+24 along the '$SKSO\ i$' and '$SKSO\ j$' axis with rates of transitions between two SKSOs represented by R_{iijj}, in units of ps^{-1}. The magnitude of each R_{iijj} component is proportional to $|\hat{V}_{ij}^{NA}(t)|^2$, per Fermi's Golden Rule. Regions on the right/left side of **Figure 2(b)** represent intra-band transitions in the conduction/valence band. There are two features of the SKSO computed Redfield tensor worth noting here: (1) Fast, resonant transitions between adjacent degenerate states $R_{i-1,i-1,jj}$ (tall peaks in **Figure 2(b)**); (2) Numerous low intensity transitions away from main diagonal $R_{i-x,i-x,jj}$ where $x > 1$.

For the excited state dynamics, we chose initial conditions based on high probability photo-excitations. For this letter we will use the HO-8 to LU+11 transitions as an example. This transition represents a $p_h' \rightarrow p_e$ type of transitions from DOS, see **Figure 1(b)**, and corresponds to the 'c' type peak in the absorption spectra, see **Figure 1(c)**. Carrier cooling after the HO-8 to LU+11 transition with energy $h\nu_{photo-excitation}$ is illustrated in **Figure 2(c).** The green color represents ground-state charge density, yellow represents gain in charge density, $\Delta n>0 = e^-$, and blue represents loss of charge density, $\Delta n<0 = h^+$. Dashed and solid curves represent average electron energy $\langle\Delta\varepsilon_e\rangle(t)$ and hole energy $\langle\Delta\varepsilon_h\rangle(t)$ during relaxation, respectively. The x-axis is a normalized log scale where 0 represents 1 ps. τ_e and τ_h represent times of relaxation from *LU+y* to *LU* and *HO-x* to *HO*. We assume single exponential energy decay curves with relaxation rate $[\tau_e]^{-1} = k_e$ and $[\tau_h]^{-1} = k_h$. Once the carriers relax to the LU/HO states there is the possibility of radiative recombination and the emission of a photon of energy $h\nu_{PL}$. We note two observations about **Figure 2(c):** (1) Both carriers show fast sub-picosecond carrier cooling on the order of 10^2 fs, which agrees with reported carrier cooling studies on $CsPbBr_3$ NCs; [38,40,41] (2) The photo-excited electron shows a long decay of hot carriers near the LU state (faint yellow smear above LU state). This feature is explored further.

Generally, hot carrier cooling rate is a function of excitation energy. If carrier cooling follows a 'gap law' type of trend then the quantity $\ln(\tau_{cooling}) \propto \Delta E_{dissipation}$ where $\Delta E_{dissipation} = \langle\Delta\varepsilon_{e/h}\rangle(t) - \langle\Delta\varepsilon_{e/h}\rangle(\infty)$. In SI **Figure S6** we plot $\ln(\tau_{cooling})$ as a function of $\Delta E_{dissiption}$ for a hot electron/hole using the SKSO basis (blue, cross/red, square) and a spin-restricted (SR) basis with no SOC interaction (green, big circle/black, small circle). The dotted lines represent a linear best fit to the computed carrier cooling curves with the parameters listed in SI **Table S3**. Lowest dissipation energy represents the LU+3/LU+2 to

LU+1/LU or HO-3/HO-2 to HO-1/HO transition for SOC calculations and LU+1 to LU or HO-1 to HO transitions for SR calculations.

The interesting quantities to compare are the cooling rates as a function of electronic basis (SKSO vs. SR). For hot hole cooling, it is seen that both the SR and SOC computed rates share similar trends and have a similar average slope for the linear fit and weakly obey gap law trends. For hot electron cooling, two different trends are observed between the SR and SOC calculations. The SR shows a trend similar to gap law while the SOC calculation shows that carrier cooling rates is slightly independent of excitation energy and is slowest for the lowest transition energy. This indicates that for hot-hole cooling, SOC has negligible effects while for hot electrons SOC significantly alters excited state dynamics.

To highlight the changes in hot electron cooling with different basis we plot the normalized energy relaxation $\langle \boldsymbol{E_e} \rangle(\boldsymbol{t})$**,** from SI equation 13, alongside relative alignment of energy bands for SKSO and SR in SI **Figure S7(a)-(b)**. The two curves plotted are of the computed energy relaxation (black, solid) and the single exponential fit (red, dotted). For SOC computed relaxation, SI **Figure 7(a)**, the early dynamics follow a single exponential decay while near the LU state the dynamics slows down dramatically. This can be attributed to the large 0.19 eV sub-gap between LU+3/LU+2 and LU+1/LU energy states. It is seen for the SR computed relaxation, SI **Figure 7(b)**, that the relaxation occurs very quickly and closely follows a single exponential decay associated with gap law. These features are explored more in the discussion section.

Up to now we have discussed the non-radiative relaxation of charge carriers. But along the excited-state trajectory, radiative relaxation mechanisms, such as carrier cooling through IR emission and radiative charge recombination, can compete with non-radiative relaxation. **Figure 2(d)** illustrates radiative relaxation along the excited state trajectory. The left part of the figure shows time resolved emission along the trajectory in $\log_{10}$ time scale and the right part shows the time-integrated emission. The initial condition is the same as that for **Figure 2(c)** with an initial photo-excitation of energy $h\nu_{photo-excitation}$ and radiative relaxation thereafter. It is seen that there are low energy IR photons emitted on the 1-100 fs timescale and after both charge carriers relax to respective HO/LU states there is bright PL. An interesting note is that even with the slow hot-electron decay near the LU state, we do not observe any hot carrier PL with energy greater than the bandgap.

The PL linewidth from the excited-state trajectory in **Figure 2(d)** is artificially narrow due to an approximation that the average PL emission will come from minima of the potential energy surfaces. To compute PL linewidth in our atomistic model, we implement a previously reported molecular dynamics photoluminescence (MDPL) protocol[42] to account for perturbations of HO-LU oscillator strength along MD trajectory. SI **Figure S8** compares the normalized PL curves of our model (red, solid) and of the experimental sample (black, dotted). The full-width half-max (FWHM) for our computational model is 56 nm and our experimental sample shows a FWHM of 18 nm. The experimental sample is consistent with other reported values of linewidths for $CsPbBr_3$ samples with mean edge length ~10nm [1,43]. We attribute the broader linewidth of the computational model to the enhanced coupling of charge carriers to surface states in our small atomistic model. Since our model has significantly larger surface area to volume ratio than experimentally observed samples, vibrational modes contributed by the surface will have a more pronounced effect on our model. Experimentally it has been observed that decreased $CsPbX_3$ size results in homogenous broadening of the PL linewidth[44], which is consistent with enhanced electron-phonon coupling. This trend is also observed with analogous chalcogenide QDs as well[45]. But, to our knowledge, it is still an open question as to whether the effect is driven by enhanced surface contributions or due to confinement of phonon modes.

To compute the PLQY, we consider a two-state model where radiative and non-radiative transition rates are determined from the Einstein coefficient for spontaneous emission, A_{ij}, and the Redfield tensor elements R_{iijj}, respectively. For the Einstein coefficient we use oscillator strengths f_{ij} that are time averaged over the MD trajectory; $< f_{ij} > \ = \frac{1}{T}\int_0^T dt f_{ij}(R(t))$ where T is the total interval of the trajectory and $R(t)$ represents ionic coordinates as function of time. Since the energy eigenvalues for the conduction and valence band edge are both twice degenerate, there are four possible transitions: LU→HO, LU+1→HO, LU→HO-1, and LU+1→HO-1. This means the terms k_{rad} and $k_{non-rad}$ will be the sum of the respective recombination rates, $\frac{\sum k_{rad}}{\sum k_{rad} + \sum k_{non-rad}}$. Values of k_{rad} and $k_{non-rad}$ for each transition are shown in **Table 2**. These rates give a resultant PLQY of 53%. Comparison of time-averaged k_{rad} to ground-state k_{rad} and relevant experiments are shown in SI **Table S4.**

Discussion

When placing the computed results of our atomistic model in context with reported experimental results in the literature, it is important to keep a few points in mind. First, we note that our fully passivated $CsPbBr_3$ atomistic model is roughly an order of magnitude smaller than what is generally seen in experiment and is ~3x smaller than the smallest NCs reported in literature. This implies that surface effects should be more pronounced than in experiment. Second, the $RCHOO^-$/RNH_3^+ organic ligands used for surface passivation are one of 3 typical configurations reported in the literature for oleic acid and oleylamine based synthesis, with the others being Cs(oleate) / RNH_2 and RNH_3^+ / Br^-. The length of the hydrocarbon chains on the acetate/ethylammonium ligands is significantly smaller than oleic acid and olylammonium ligands in experiment as well. Lastly, our excited-state dynamics methodology treats photo-induced charge carriers as independent particles coupled to phonon modes, neglecting Coulombic interactions. This implies that our excited-state calculations should be comparable to experiments with low carrier densities $\langle N \rangle < 1$.

It is generally known that electronic structure calculations based on DFT applied to $APbX_3$ perovskites using the GGA functional without including SOC bandgaps roughly corresponds experimentally determined bandgaps because of a cancelation of errors. For our $Cs_8Pb_{27}Br_{54}$ model, when only a GGA functional is used, a bandgap of 3.12 eV is found. With the inclusion of SOC the gap reduces to 2.38 eV, a difference of 0.74 eV, which is in good agreement to what has been reported previously.[15, 46] This gives a bandgap which resembles $CsPbBr_3$ NCs in the intermediate confinement regime with an edge length of ~10 nm. Although it is accidental that the computed bandgap with GGA+SOC is very similar to experiment, it is a convenient accident for excited-state dynamics calculations, since rates of recombination across the bandgap depend inversely on the bandgap energy.

Generally, for dipole-induced transitions, selection rules forbid transitions to envelope functions that have opposite parity, such as $s_h \rightarrow p_e$. These restrictions are relaxed when symmetries, such as rotational or inversion, are broken. In the case of $APbX_3$ NCs it is generally known that inversion symmetry of the crystal lattice is distorted due to the observation of Rashba effects.[47-48]. This also indicates that selection rules may be relaxed in $APbX_3$ NCs due to symmetry breaking of the crystal lattice. From the computed spectra shown in **Figure 1(c)** it is observed that in the 'b' region where asymmetric $s_h \rightarrow p_e$ or $p_h \rightarrow s_e$ are expected, a spectral feature appears, which we attribute to symmetry breaking.

To understand how computational methodology impacts computed excited-state dynamics observables, we compare SKSO and SR computed Redfield tensors. The SR Redfield tensor is shown in SI **Figure S9**. For the SR tensor, most of the transitions are located within regions $R_{i-x,i-x,jj}$ where $x < 3$. It is expected that the SKSO computed tensor should provide more off-diagonal state-to-state transitions than the SR for two reasons: (1) NCL spin basis used to generate SKSOs should effectively increase the local density of non-adiabatic transitions within an energy window of $kT \approx 26\ meV$ for thermal relaxation; (2) Inclusion of SOC should mix spin states of the SKSOs which allows for spin forbidden transitions which are not allowed in the SR basis. SI **Figure S10** shows the number of transitions to each *HO-x* and *LU+y* state for SKSO (blue) and SR (orange) basis with rate above $1\ ps^{-1}$. It is observed that SKSO basis has roughly 2 times as many transitions for a given state than SR. It is also noted that for LU states, there are more transition states than for HO states. This can be attributed to greater SOC interactions in conduction band states (Pb-6p) as compared to valence band states (Pb-6s, Br-4p).

The SOC interaction has a more significant impact on hot-electron relaxation than hot-hole relaxation due to the intrinsic electronic structure of perovskite $APbX_3$ materials. The valence band is composed of hybridized Br *4p*/Pb *6s* atomic orbitals while the conduction band is composed of hybridized Pb *6p* orbitals. Up to 1st order in atomic orbital basis, the $L \cdot S$ interaction, from SI equation 7, lowers the particles energy ΔE_{SOC} by a factor proportional to $\frac{Z^4}{n^3}$ where Z is the atomic number and n is the principle quantum number. For Pb(Z = 82, n =6) and Br(Z = 35, n = 4) this gives $\frac{\Delta E_{SOC}(Pb)}{\Delta E_{SOC}(Br)} \propto 8.93$. This implies that there should be roughly an order of magnitude greater energy splitting in the conduction band edge states than the valence band edge states, which is what we observe with our DFT based calculations.

From the two-state model of radiative and non-radiative recombination we found that the fully passivated $Cs_8Pb_{27}Br_{54}$ NC with time-averaged k_{rad} and $k_{non-rad}$ showed a PLQY of 53%. For conventional II-IV and III-V QDs, complete surface passivation is needed for bright PL emission due to dangling bonds localized on the surface resulting in deep-trap states.[49] For $APbX_3$ perovskites, it has been found that dangling bonds are not as detrimental to high PLQY emission due to a unique bonding character near the valence and conduction band edges[50] that gives them a high defect tolerance. Heuristically, since we did not observe ligands desorbing from the NC surface during MD, we expect that our fully passivated NC should provide near unity PLQY, as seen in experiment. Our computed PLQY = 53% is not unreasonable but is lower than expectations.

The lower than expected PLQY can be attributed to the fact that $k_{rad} \approx k_{non\text{-}rad}$ in our simulation (**Table 2**). To achieve near unity PLQY, through bi-molecular recombination, it is required that $k_{rad} >> k_{non\text{-}rad}$. For $k_{non\text{-}rad}$, we suspect that it is a function of surface termination (ligand type) and NC size, with the two not necessarily being mutually exclusive features. We raise a few possibilities which could impact k_{rad} and $k_{non-rad}$. First, during the MD trajectory, oscillator strengths will vary due to bond elongation/contraction. Elongation of Pb-O bonds at the surface can produce momentary trap states that quench the oscillator strength. Second, non-radiative energy dissipation is dependent on phonon frequencies coupled to electronic states. It has been shown that passivating ligands can contribute to the spectral density and enhance carrier cooling in NCs and QDs.[51] As we have already noted, we observe homogenous broadening of the PL linewidth with decreased NC size, which has also been reported in the literature. Homogeneous broadening implies enhanced nonadiabatic coupling which drives non-radiative recombination. Also, our atomistic model uses a Pb-$RCOO^-$ passivation while a Pb-Br termination is also possible. It would be expected that the Pb-O vibrational modes have higher frequencies than Pb-Br vibrational modes, providing enhanced nonadiabatic coupling. With increased NC size, a greater proportion of the electron and hole charge density would be coupled to the 'interior' of the NC (and less coupled to surface vibrational modes), which has a more crystalline structure. This should result in reduced symmetry-breaking and slower non-radiative recombination. Other atomistic studies have also found that nonradiative recombination is altered due to the type of passivation ligands, with inorganic passivation and Lewis bases providing significantly lower nonradiative recombination rates.[52,53] Thus, we suspect that a Br^-/RNH_3^+ passivation would provide a PLQY closer to 100% due to the slower ionic motion of Br^- compared to the $RCHOO^-$ ligand. Another possibility is that the surface electron-phonon coupling is a function of the hydrocarbon chain length of the organic passivating ligand. Long chain hydrocarbons would have less degrees of freedom and smaller range for available amplitudes for vibrational motion due to interacting with neighboring ligands, while short chain ligands are less impacted by steric interactions. A final note is that we neglect the Rashba effect on $k_{non-rad}$ and k_{rad}as it would require computing momentum unrestricted NACs and oscillator strengths, which is currently in development [54]. Theory predicts that the Rashba effect would slightly slow down $k_{non-rad}$[55] and k_{rad}[12] since our model is in the strong confinement regime.

During the excited state dynamics trajectory, after a steady state $p_h' \rightarrow p_e$ optical transition, it was observed that hot electron cooling is slowed down near the band edge and displayed 2nd order kinetics due to the large sub-gap between LU/LU+1 and higher energy states. For larger NCs the sub-gap would likely become smaller due to the DOS becoming denser near the band edge, with single decay kinetics. In a recent transient absorption experiment, carrier cooling was explored in the low carrier density regime ($\langle N \rangle = 0.1$) for various sizes (5nm, 9nm, and 12nm) of CH_3NH_3PbBr3 NCs with an excitation energy of 3.1 eV [10]. This transition energy is comparable to the 3.01 eV $p_h' \rightarrow p_e$ transition explored here. The experimental data suggests that with decreasing size, carrier cooling slows down near the band edge. This seems to support our claim that the combination of giant SOC and a sparse DOS near the band edge slows down carrier cooling in $APbX_3$ NCs.

Before concluding we provide some suggestions on the rational design of perovskite NC-solid devices. In the single-excitation limit (i.e. a single electron and hole), radiative recombination is expected to be enhanced with greater electronic confinement and would be beneficial for LEDs. We note three reasons why we think strongly-confined $CsPbX_3$ NCs are not ideal materials for LEDs. First, in the single-particle simulations, we observe that hot-electron cooling slows down with enhanced confinement due to a large SOC interaction creating sub-gaps in the conduction band. This is not ideal, as extending the carrier cooling time delays radiative electron-hole recombination. Second, under practical operating conditions, NC based LEDs operate in the many-body regime (multiple excited electrons and holes per NC) which introduce competing non-radiative relaxation mechanisms, such as Auger recombination (heating). Auger recombination is enhanced by confinement and is an order of magnitude faster than radiative recombination. This has been found to be one of the main causes of the observed ‘efficiency drop’ above a threshold current intensity[56-58]. Lastly, it has been theorized for $CsPbX_3$ NCs with enhanced confinement that the radiative recombination rate is slowed down due to competition between the Rashba effect and Coulomb interaction.[12] This last point is still an open question within the community.

For NC based photovoltaics, we expect that strongly-confined $CsPbX_3$ NCs could be more optimal than intermediately-confined NCs for the following reasons. First, in the non-interacting single-particle simulations, the observed delay of hot-electron cooling would be beneficial as it also delays radiative and non-radiative recombination, extending the charge-carriers lifetime and allowing for more pathways to transfer from perovskite layer to the electron/hole transport layer. Second, when multi-body interactions are taken into account, multi-exciton generation (MEG) becomes an efficient process,[10-11, 59] turning a single high-energy charge carrier into two lower-energy charge carriers and allowing for PV efficiency to increase above the Shockley-Queisser limit. Combining the facts that the efficiency of MEG depends on the bandgap while high dielectric screening mitigates enhanced Coulomb interaction between charges for small NCs,[60] the optimal choice is likely to be NC sizes that are comparable to the Bohr radii. This argument neglects the role of charge transport in NC based PVs, which is beyond the scope of this work, but we comment that coupling between NCs can be modified by ligand exchange methods which include reducing the length of insulating ligand chain[61] or by introducing conductive ligands.[62]

Conclusions

In conclusion, we use spinor Kohn-Sham orbitals (SKSOs) as a basis to compute excited-state dissipative dynamics in a fully-passivated $CsPbBr_3$ NC using Redfield theory in density matrix formalism to describe electron-phonon interactions. From the rates k_{rad} and $k_{non-rad}$ we computed a PLQY of 53%, which is lower than what would be expected for a fully surface passivated NC without surface trap states. This indicates that surface termination and NC size plays an important role in determining PLQY. We attribute the lower than expected PLQY value to enhancement of $k_{non-rad}$ through additional degrees of freedom and the normal modes of short-chain passivation ligand used for the atomistic model. Computed PL linewidths of the atomistic model are ~3x larger than our ensemble measurements on NCs approximately 10nm in edge length. This is also attributed to enhanced coupling to surface phonons. Computed hot carrier cooling rates compared favorably to reports in the literature of fast sub-picosecond cooling on the scale of ~300 fs under low excitation densities. With the inclusion of SOC in excited-state dissipative dynamics, it was observed that *nonadiabatic coupling* was enhanced, which has been reported in calculations of bulk $MAPbI_3$, but hot electron cooling was slowed down, which we attribute to a large (~0.20 eV) non-resonant sub-gap above the conduction band edge and a subsequent "*phonon bottleneck*".

VI. ACKNOWLEDGEMENTS

Authors acknowledge the use of computational resources at the Center for Computationally Assisted Science and Technology (CCAST) at North Dakota State University. Authors thank DOE BES NERSC facility for computational resources via allocation award *#31857*, "*Computational Modeling of Photo-catalysis and Photo-induced Charge Transfer Dynamics on Surfaces*" supported by the Office of Science of the DOE under contract no. DE-AC02-05CH11231. DSK acknowledges support of NASF CHE-1800476 for computational methods development. The work of I.T.M. is performed under the state assignment of IGM SB RAS. T.M.I. gratefully acknowledges financial support of the Ministry of Education and Science of the Russian Federation in the framework of the Increase Competitiveness Program of NUST MISIS (No. K3-2018-022) implemented by a governmental decree dated 16th of March 2013, N 211. The calculations were partially performed at supercomputer cluster "Cherry" provided by the Materials Modeling and Development Laboratory at NUST "MISIS" (supported via the Grant from the Ministry of

Education and Science of the Russian Federation No. 14.Y26.31.0005). AF and DSK thank S. Tretiak, F. Furche, S. Kilina, Y. Han, L. Johnson, M. Jabed, L. Lystrom for discussions.

VII. Supporting Information

Supporting Information Available: Synthesis of $CsPbBr_3$ NCs, spectral characterization of $CsPbBr_3$ NCs, details of the computational methods, structural characterization of atomistic models showing tabulated bond distances and radial distribution functions, a table of DOS transitions and absorption spectrum peaks, log plot of computed and experimental absorption spectrum, KSO energy fluctuations along MD trajectory, spin-restricted Redfield tensor, histogram of state-to-state transitions for KSO and SKSO, hot carrier cooling as a function of dissipation energy, a table of linear fits to hot carrier cooling curves, a comparison of hot electron cooling in SKSO and KSO basis, snapshots of spatial occupations of hot carriers along excited-state trajectory, comparing computed MDPL linewidths to experimental samples, and comparison of computed radiative recombination rate to reported experimental values.

This material is available free of charge via the Internet at http://pubs.acs.org

VIII. References

1. Protesescu, L.; Yakunin, S.; Bodnarchuk, M. I.; Krieg, F.; Caputo, R.; Hendon, C. H.; Yang, R. X.; Walsh, A.; Kovalenko, M. V., Nanocrystals of Cesium Lead Halide Perovskites (CsPbX(3), X = Cl, Br, and I): Novel Optoelectronic Materials Showing Bright Emission with Wide Color Gamut. *Nano Lett.* **2015,** *15*, 3692-3696.
2. Beard, M. C.; Luther, J. M.; Nozik, A. J., The Promise and Challenge of Nanostructured Solar Cells. *Nat. Nanotechnol.* **2014,** *9*, 951-954.
3. He, J.; Vasenko, A. S.; Long, R.; Prezhdo, O. V., Halide Composition Controls Electron–Hole Recombination in Cesium–Lead Halide Perovskite Quantum Dots: A Time Domain Ab Initio Study. *J. Phys. Chem. Lett.* **2018,** *9*, 1872-1879.
4. Madjet, M. E.; Berdiyorov, G. R.; El-Mellouhi, F.; Alharbi, F. H.; Akimov, A. V.; Kais, S., Cation Effect on Hot Carrier Cooling in Halide Perovskite Materials. *J. Phys. Chem. Lett.* **2017,** *8*, 4439-4445.
5. Hopper, T. R.; Gorodetsky, A.; Frost, J. M.; Müller, C.; Lovrincic, R.; Bakulin, A. A., Ultrafast Intraband Spectroscopy of Hot-Carrier Cooling in Lead-Halide Perovskites. *ACS Energy Lett.* **2018,** *3*, 2199-2205.
6. Evans, T. J. S.; Miyata, K.; Joshi, P. P.; Maehrlein, S.; Liu, F.; Zhu, X. Y., Competition Between Hot-Electron Cooling and Large Polaron Screening in CsPbBr3 Perovskite Single Crystals. *J. Phys. Chem. C* **2018,** *122*, 13724-13730.
7. Park, M.; Neukirch, A. J.; Reyes-Lillo, S. E.; Lai, M.; Ellis, S. R.; Dietze, D.; Neaton, J. B.; Yang, P.; Tretiak, S.; Mathies, R. A., Excited-State Vibrational Dynamics Toward the Polaron in Methylammonium Lead Iodide Perovskite. *Nat. Commun.* **2018,** *9*, 2525-9.
8. Miyata, K.; Meggiolaro, D.; Trinh, M. T.; Joshi, P. P.; Mosconi, E.; Jones, S. C.; De Angelis, F.; Zhu, X. Y., Large Polarons in Lead Halide Perovskites. *Sci. Adv.* **2017,** *3,* e1701217.
9. Li, M.; Bhaumik, S.; Goh, T. W.; Kumar, M. S.; Yantara, N.; Grätzel, M.; Mhaisalkar, S.; Mathews, N.; Sum, T. C., Slow Cooling and Highly Efficient Extraction of Hot Carriers in Colloidal Perovskite Nanocrystals. *Nat. Commun.* **2017,** *8*, 14350.
10. Li, M.; Begum, R.; Fu, J.; Xu, Q.; Koh, T. M.; Veldhuis, S. A.; Grätzel, M.; Mathews, N.; Mhaisalkar, S.; Sum, T. C., Low Threshold and Efficient Multiple Exciton Generation in Halide Perovskite Nanocrystals. *Nat. Commun.* **2018,** *9*, 4197.
11. Vogel, D. J.; Kryjevski, A.; Inerbaev, T.; Kilin, D. S., Photoinduced Single- and Multiple-Electron Dynamics Processes Enhanced by Quantum Confinement in Lead Halide Perovskite Quantum Dots. *J. Phys. Chem. Lett.* **2017,** *8*, 3032-3039.
12. Becker, M. A.; Vaxenburg, R.; Nedelcu, G.; Sercel, P. C.; Shabaev, A.; Mehl, M. J.; Michopoulos, J. G.; Lambrakos, S. G.; Bernstein, N.; Lyons, J. L.; Stöferle, T.; Mahrt, R. F.; Kovalenko, M. V.; Norris, D. J.; Rainò, G.; Efros, A. L., Bright Triplet Excitons in Caesium Lead Halide Perovskites. *Nature* **2018,** *553*, 189.
13. Kang, J.; Wang, L.-W., High Defect Tolerance in Lead Halide Perovskite CsPbBr3. *J. Phys. Chem. Lett.* **2017,** *8*, 489-493.
14. Walsh, A.; Scanlon, D. O.; Chen, S.; Gong, X. G.; Wei, S.-H., Self-Regulation Mechanism for Charged Point Defects in Hybrid Halide Perovskites. *Angew. Chem. Int. Ed.* **2014,** *54*, 1791-1794.
15. Even, J.; Pedesseau, L.; Jancu, J.-M.; Katan, C., Importance of Spin–Orbit Coupling in Hybrid Organic/Inorganic Perovskites for Photovoltaic Applications. *J. Phys. Chem. Lett.* **2013,** *4*, 2999-3005.
16. Umari, P.; Mosconi, E.; De Angelis, F., Relativistic GW calculations on CH3NH3PbI3 and CH3NH3SnI3 Perovskites for Solar Cell Applications. *Sci. Rep.* **2014,** *4, 4467.*

17. Li, W.; Zhou, L.; Prezhdo, O. V.; Akimov, A. V., Spin–Orbit Interactions Greatly Accelerate Nonradiative Dynamics in Lead Halide Perovskites. *ACS Energy Lett.* **2018,** *3*, 2159-2166.

18. Bockelmann, U.; Bastard, G., Phonon Scattering and Energy Relaxation in Two-, One-, and Zero-Dimensional Electron Gases. *Phys. Rev. B* **1990,** *42*, 8947-8951.

19. Geiregat, P.; Maes, J.; Chen, K.; Drijvers, E.; De Roo, J.; Hodgkiss, J. M.; Hens, Z., Using Bulk-like Nanocrystals To Probe Intrinsic Optical Gain Characteristics of Inorganic Lead Halide Perovskites. *ACS Nano.* **2018,** *12*, 10178-10188.

20. Jia, X.; Jiang, J.; Zhang, Y.; Qiu, J.; Wang, S.; Chen, Z.; Yuan, N.; Ding, J., Observation of Enhanced Hot Phonon Bottleneck Effect in 2D Perovskites. *Appl. Phys. Lett.* **2018,** *112*, 143903.

21. Yang, Y.; Ostrowski, D. P.; France, R. M.; Zhu, K.; van de Lagemaat, J.; Luther, J. M.; Beard, M. C., Observation of a Hot-Phonon Bottleneck in Lead-Iodide Perovskites. *Nat. Photonics* **2015,** *10*, 53.

22. Yang, J.; Wen, X.; Xia, H.; Sheng, R.; Ma, Q.; Kim, J.; Tapping, P.; Harada, T.; Kee, T. W.; Huang, F.; Cheng, Y.-B.; Green, M.; Ho-Baillie, A.; Huang, S.; Shrestha, S.; Patterson, R.; Conibeer, G., Acoustic-Optical Phonon Up-Conversion and Hot-Phonon Bottleneck in Lead-Halide Perovskites. *Nat. Commun.* **2017,** *8*, 14120.

23. Maes, J.; Balcaen, L.; Drijvers, E.; Zhao, Q.; De Roo, J.; Vantomme, A.; Vanhaecke, F.; Geiregat, P.; Hens, Z., Light Absorption Coefficient of CsPbBr3 Perovskite Nanocrystals. *J. Phys. Chem. Lett.* **2018,** *9*, 3093-3097.

24. Almeida, G.; Goldoni, L.; Akkerman, Q.; Dang, Z.; Khan, A. H.; Marras, S.; Moreels, I.; Manna, L., Role of Acid–Base Equilibria in the Size, Shape, and Phase Control of Cesium Lead Bromide Nanocrystals. *ACS Nano.* **2018,** *12*, 1704-1711.

25. Perdew, J. P.; Burke, K.; Ernzerhof, M., Generalized Gradient Approximation Made Simple. *Phys. Rev. Lett.* **1997,** *78*, 1396-1396.

26. Blöchl, P. E., Projector Augmented-Wave Method. *Phys. Rev. B* **1994,** *50*, 17953-17979.

27. Kresse, G.; Joubert, D., From Ultrasoft Pseudopotentials to the Projector Augmented-Wave Method. *Phys. Rev. B* **1999,** *59*, 1758-1775.

28. Kresse, G.; Furthmuller, J., Efficiency of Ab-initio Total Energy Calculations for Metals and Semiconductors Using a Plane-Wave Basis Set. *Comput. Mater. Sci.* **1996,** *6*, 15-50.

29. Inerbaev, T. M.; Hoefelmeyer, J. D.; Kilin, D. S., Photoinduced Charge Transfer from Titania to Surface Doping Site. *J. Phys. Chem. C.* **2013,** *117*, 9673-9692.

30. Forde, A.; Kilin, D., Hole Transfer in Dye-Sensitized Cesium Lead Halide Perovskite Photovoltaics: Effect of Interfacial Bonding. *J. Phys. Chem. C.* **2017,** *121*, 20113-20125.

31. Han, P.; Bester, G., First-Principles Calculation of the Electron-Phonon Interaction in Semiconductor Nanoclusters. *Phys. Rev. B* **2012,** *85, 235422.*

32. Kryjevski, A.; Mihaylov, D.; Kilina, S.; Kilin, D., Multiple Exciton Generation in Chiral Carbon Nanotubes: Density Functional Theory Based Computation. *J. Chem. Phys.* **2017,** *147*, 154106.

33. Giustino, F., Electron-Phonon Interactions From First Principles. *Rev. Mod. Phys.* **2017,** *89*, 015003.

34. Redfield, A. G., On the Theory of Relaxation Processes. *IBM J. Res. Dev.* **1957,** *1*, 19-31.

35. Jean, J. M.; Friesner, R. A.; Fleming, G. R., Application of a Multilevel Redfield Theory to Electron Transfer in Condensed Phases. *J. Chem. Phys.* **1992,** *96*, 5827-5842.

36. Einstein, A., On the Quantum Theory of Radiation. *Physikalische Zeitschrift* **1917,** *18,* 121.

37. Kilina, S.; Ivanov, S.; Tretiak, S., Effect of Surface Ligands on Optical and Electronic Spectra of Semiconductor Nanoclusters. *J. Am. Chem. Soc.* **2009,** *131*, 7717-7726.

38. Makarov, N. S.; Guo, S.; Isaienko, O.; Liu, W.; Robel, I.; Klimov, V. I., Spectral and Dynamical Properties of Single Excitons, Biexcitons, and Trions in Cesium-Lead-Halide Perovskite Quantum Dots. *Nano Lett.* **2016,** *16*, 2349-2362.

39. Brennan, M. C.; Herr, J. E.; Nguyen-Beck, T. S.; Zinna, J.; Draguta, S.; Rouvimov, S.; Parkhill, J.; Kuno, M., Origin of the Size-Dependent Stokes Shift in CsPbBr3 Perovskite Nanocrystals. *J. Am. Chem. Soc.* **2017,** *139*, 12201-12208.
40. Telfah, H.; Jamhawi, A.; Teunis, M. B.; Sardar, R.; Liu, J., Ultrafast Exciton Dynamics in Shape-Controlled Methylammonium Lead Bromide Perovskite Nanostructures: Effect of Quantum Confinement on Charge Carrier Recombination. *J. Phys. Chem. C* **2017,** *121*, 28556-28565.
41. Chung, H.; Jung, S. I.; Kim, H. J.; Cha, W.; Sim, E.; Kim, D.; Koh, W.-K.; Kim, J., Composition-Dependent Hot Carrier Relaxation Dynamics in Cesium Lead Halide (CsPbX3, X=Br and I) Perovskite Nanocrystals. *Angew. Chem. Int. Ed.* **2017,** *56*, 4160-4164.
42. Vogel, D. J.; Kilin, D. S., First-Principles Treatment of Photoluminescence in Semiconductors. *J. Phys. Chem. C* **2015,** *119*, 27954-27964.
43. Krieg, F.; Ochsenbein, S. T.; Yakunin, S.; ten Brinck, S.; Aellen, P.; Süess, A.; Clerc, B.; Guggisberg, D.; Nazarenko, O.; Shynkarenko, Y.; Kumar, S.; Shih, C.-J.; Infante, I.; Kovalenko, M. V., Colloidal CsPbX3 (X = Cl, Br, I) Nanocrystals 2.0: Zwitterionic Capping Ligands for Improved Durability and Stability. *ACS Energy Lett.* **2018,** *3*, 641-646.
44. Utzat, H.; Shulenberger, K. E.; Achorn, O. B.; Nasilowski, M.; Sinclair, T. S.; Bawendi, M. G., Probing Linewidths and Biexciton Quantum Yields of Single Cesium Lead Halide Nanocrystals in Solution. *Nano Lett.* **2017,** *17*, 6838-6846.
45. Gellen, T. A.; Lem, J.; Turner, D. B., Probing Homogeneous Line Broadening in CdSe Nanocrystals Using Multidimensional Electronic Spectroscopy. *Nano Lett.* **2017,** *17*, 2809-2815.
46. Filip, M. R.; Giustino, F., GW Quasiparticle Band Gap of the Hybrid Organic-Inorganic Perovskite CH3NH3PbI3: Effect of Spin-Orbit Interaction, Semicore Electrons, and Self-Consistency. *Phys.Rev. B* **2014,** *90, 245145.*
47. Isarov, M.; Tan, L. Z.; Bodnarchuk, M. I.; Kovalenko, M. V.; Rappe, A. M.; Lifshitz, E., Rashba Effect in a Single Colloidal CsPbBr3 Perovskite Nanocrystal Detected by Magneto-Optical Measurements. *Nano Lett.* **2017,** *17*, 5020-5026.
48. Mosconi, E.; Etienne, T.; De Angelis, F., Rashba Band Splitting in Organohalide Lead Perovskites: Bulk and Surface Effects. *J. Phys. Chem. Lett.* **2017,** *8*, 2247-2252.
49. Houtepen, A. J.; Hens, Z.; Owen, J. S.; Infante, I., On the Origin of Surface Traps in Colloidal II–VI Semiconductor Nanocrystals. *Chem. Mater.* **2017,** *29*, 752-761.
50. Brandt, R. E.; Poindexter, J. R.; Gorai, P.; Kurchin, R. C.; Hoye, R. L. Z.; Nienhaus, L.; Wilson, M. W. B.; Polizzotti, J. A.; Sereika, R.; Žaltauskas, R.; Lee, L. C.; MacManus-Driscoll, J. L.; Bawendi, M.; Stevanović, V.; Buonassisi, T., Searching for "Defect-Tolerant" Photovoltaic Materials: Combined Theoretical and Experimental Screening. *Chem. Mater.* **2017,** *29*, 4667-4674.
51. Kilina, S.; Velizhanin, K. A.; Ivanov, S.; Prezhdo, O. V.; Tretiak, S., Surface Ligands Increase Photoexcitation Relaxation Rates in CdSe Quantum Dots. *ACS Nano.* **2012,** *6*, 6515-6524.
52. Liu, L.; Fang, W.-H.; Long, R.; Prezhdo, O. V., Lewis Base Passivation of Hybrid Halide Perovskites Slows Electron–Hole Recombination: Time-Domain Ab Initio Analysis. *J. Phys. Chem. Lett.* **2018,** *9*, 1164-1171.
53. Yazdani, N.; Bozyigit, D.; Vuttivorakulchai, K.; Luisier, M.; Infante, I.; Wood, V., Tuning Electron–Phonon Interactions in Nanocrystals through Surface Termination. *Nano Lett.* **2018,** *18*, 2233-2242.
54. Fatima; Vogel, D. J.; Han, Y.; Inerbaev, T. M.; Oncel, N.; Kilin, D. S., First-Principles Study of Electron Dynamics with Explicit Treatment of Momentum Dispersion on Si Nanowires Along Different Directions. *Mol. Phys.* **2018**, 1-10.
55. Pedesseau, L.; Sapori, D.; Traore, B.; Robles, R.; Fang, H. H.; Loi, M. A.; Tsai, H.; Nie, W.; Blancon, J. C.; Neukirch, A.; Tretiak, S.; Mohite, A. D.; Katan, C.; Even, J.; Kepenekian, M., Advances and Promises of Layered Halide Hybrid Perovskite Semiconductors. *ACS Nano.* **2016,** *10*, 9776-9786.

56. Cragg, G. E.; Efros, A. L., Suppression of Auger Processes in Confined Structures. *Nano Lett.* **2010,** *10*, 313-317.

57. Lim, J.; Park, Y.-S.; Wu, K.; Yun, H. J.; Klimov, V. I., Droop-Free Colloidal Quantum Dot Light-Emitting Diodes. *Nano Lett.* **2018,** *18*, 6645-6653.

58. Chang, J. H.; Park, P.; Jung, H.; Jeong, B. G.; Hahm, D.; Nagamine, G.; Ko, J.; Cho, J.; Padilha, L. A.; Lee, D. C.; Lee, C.; Char, K.; Bae, W. K., Unraveling the Origin of Operational Instability of Quantum Dot Based Light-Emitting Diodes. *ACS Nano.* **2018,** *12*, 10231-10239.

59. Beard, M. C.; Luther, J. M.; Semonin, O. E.; Nozik, A. J., Third Generation Photovoltaics based on Multiple Exciton Generation in Quantum Confined Semiconductors. *Acc. Chem. Res.* **2013,** *46*, 1252-1260.

60. Blancon, J. C.; Stier, A. V.; Tsai, H.; Nie, W.; Stoumpos, C. C.; Traoré, B.; Pedesseau, L.; Kepenekian, M.; Katsutani, F.; Noe, G. T.; Kono, J.; Tretiak, S.; Crooker, S. A.; Katan, C.; Kanatzidis, M. G.; Crochet, J. J.; Even, J.; Mohite, A. D., Scaling Law for Excitons in 2D Perovskite Quantum Wells. *Nat. Commun.* **2018,** *9*, 2254.

61. Wheeler, L. M.; Sanehira, E. M.; Marshall, A. R.; Schulz, P.; Suri, M.; Anderson, N. C.; Christians, J. A.; Nordlund, D.; Sokaras, D.; Kroll, T.; Harvey, S. P.; Berry, J. J.; Lin, L. Y.; Luther, J. M., Targeted Ligand-Exchange Chemistry on Cesium Lead Halide Perovskite Quantum Dots for High-Efficiency Photovoltaics. *J. Am. Chem. Soc.* **2018,** *140*, 10504-10513.

62. Vickers, E. T.; Graham, T. A.; Chowdhury, A. H.; Bahrami, B.; Dreskin, B. W.; Lindley, S.; Naghadeh, S. B.; Qiao, Q.; Zhang, J. Z., Improving Charge Carrier Delocalization in Perovskite Quantum Dots by Surface Passivation with Conductive Aromatic Ligands. *ACS Energy Lett.* **2018,** *3*, 2931-2939.

FIGURES AND TABLES

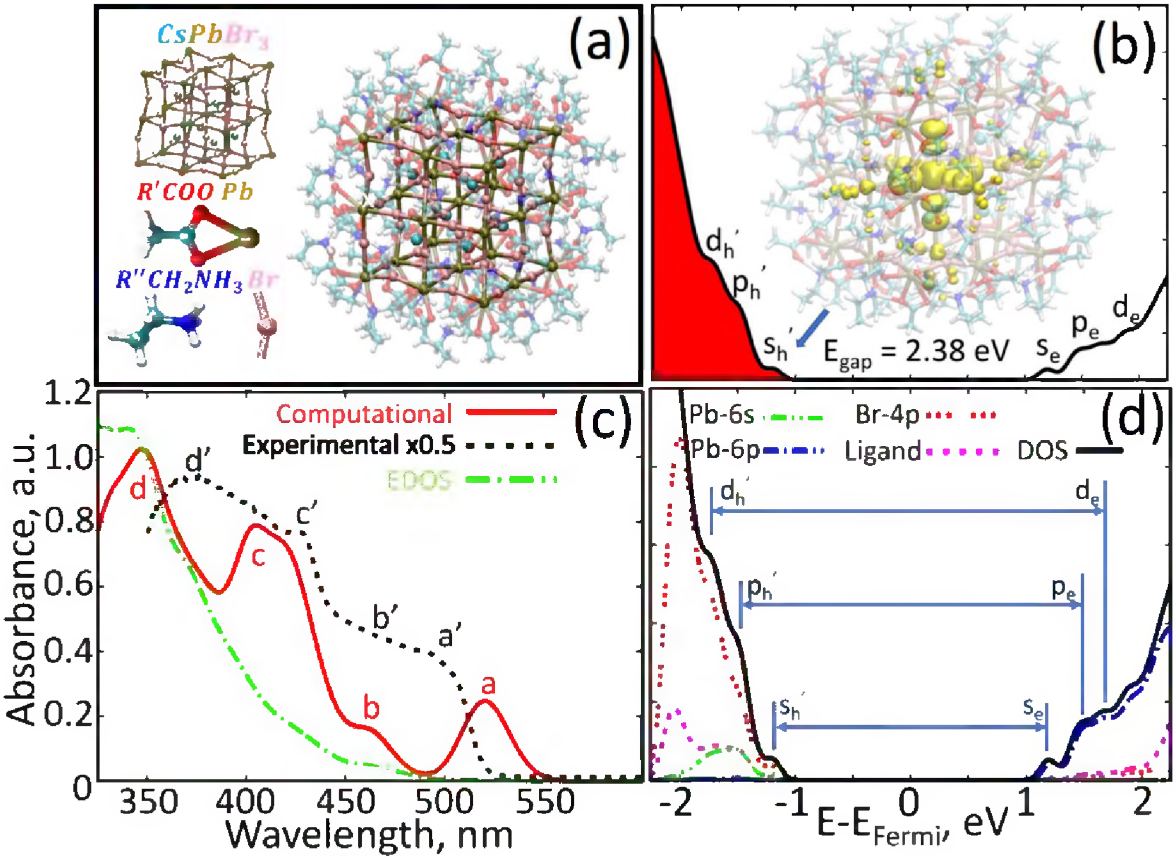

Figure 1: **(a)** Atomistic model of fully passivated $CsPbBr_3$ NC investigated in this work (Cs=light blue, Pb=brown, Br=pink). The NC is composed of a 2x2x2 unit cell of $CsPbBr_3$ carved from the bulk cubic phase with a Pb-Br terminated surface. To passivate the NC a deprotonated carboxylic acid (red) is coordinated to surface Pb^{2+} sites with a distribution of mono and bidentate arrangements and protonated amines (dark blue) coordinate with surface Br^-. **(b)** DOS of the NC computed in SKSO basis giving a bandgap of 2.38 eV. There are no states inside the bandgap indicating the NC is properly passivated. The inset shows the isosurface of the HOMO state with the electron density residing inside the $CsPbBr_3$ NC. **(c)** Computed absorption (red, solid), experimental spectra (black, dotted), and EDOS (green, line-dot). EDOS represents the density of possible optical transitions while computed absorption spectra weights each transition with the associated oscillator strength. Relevant features are alphabetically labeled (primes corresponding to experiment data) and described in the main text. **(d)** pDOS corresponding to DOS from **(b)**. Valence band has the expected hybridization between Br-4p (red, dot space dot) and Pb-6s (green, dot line) along with a contribution from the passivating ligands (pink, dotted). Conduction band is composed of Pb-6p states with negligible ligand contribution within 1 eV of band edge.

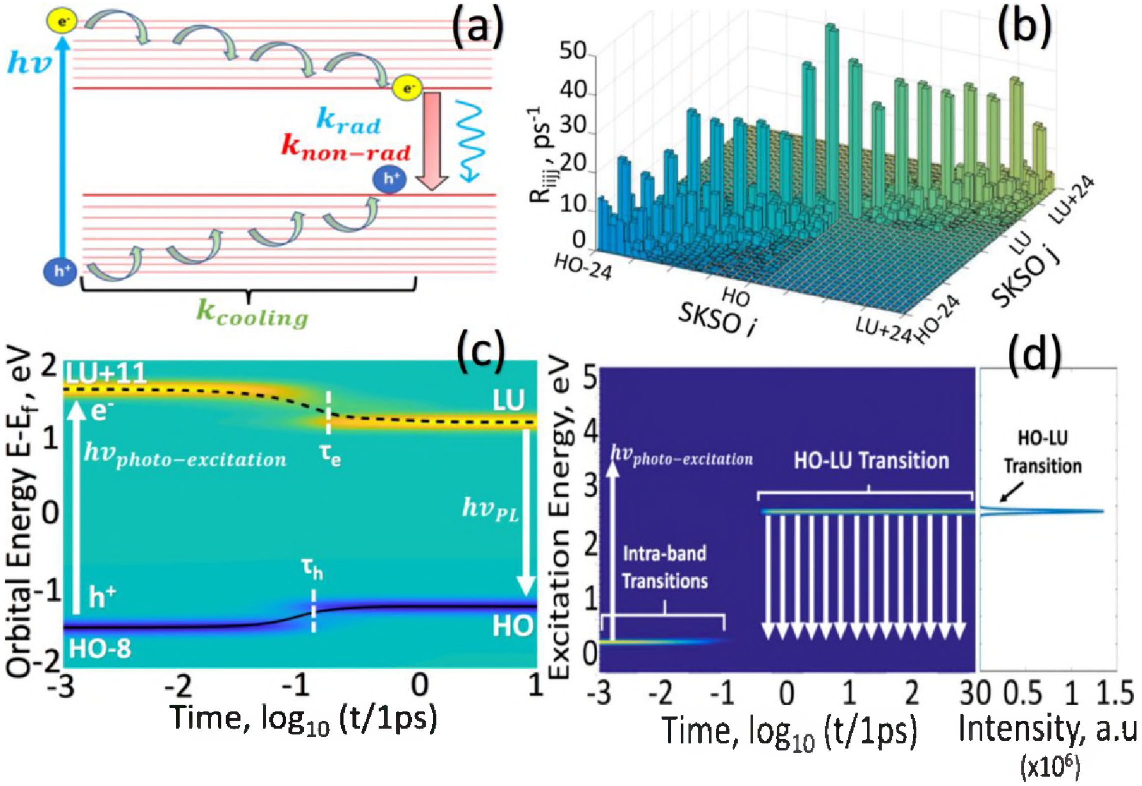

Figure 2: **(a)** Schematic of the photo-induced excited-state dynamics investigated in this work. A photo-excitation generates a photo-excited electron in the conduction band and a photo-induced hole in the valence band. On a picosecond timescale, hot carriers cool to LU/HO states by dissipating heat though NAC with phonon modes of the NC, with rate $k_{cooling}$. On a nanosecond timescale, free carriers recombine through radiative/non-radiative channels with rates $k_{non-rad}$ and k_{rad}. **(b)** SKSO computed Redfield tensor representing hot carrier cooling. Tensor elements, in units of 1/ps, describe state-to-state transitions of populations due to NAC. Comparison to SR computed Redfield tensor is shown in SI **Figure S9** and discussed in main text. **(c)** Hot carrier cooling for the specific optical transition HO-8 to LU+11 which is a bright d_h' → d_e type transition. Green represents background reference, yellow represents average occupation of charge in the conduction band, and blue represents average occupation of charge in the valence band. Horizontal dotted/solid lines represent energy expectation values of charge carriers and vertical dashed lines represent hot carrier cooling, $\tau_{cooling}$. **(d)** Time resolved and time integrated PL along the excited state trajectory corresponding to **Figure 2(c).** Before cooling to HO/LU states, hot carriers can emit low energy IR photons to dissipate energy which competes with non-radiative transitions. Once carriers relax to HO/LU states, the NC emits PL in the visible spectrum.

HO-x	LU+y	E_{trans}, eV	$\lambda_{transition}, nm$	f_{ij}	symmetry label
HO	LU+1	2.40	517	1.00	s_h-->s_e
HO-10	LU+9	3.07	405	0.60	p_h-->p_e
HO-1	LU+1	2.40	517	0.58	s_h-->s_e
HO	LU	2.40	517	0.50	s_h-->s_e
HO-1	LU	2.40	517	0.28	s_h-->s_e
HO-8	LU+10	3.11	399	0.28	p_h-->p_e
HO-2	LU+14	3.08	402	0.26	p_h-->d_e
HO-8	LU+2	2.87	432	0.24	d_h->p_e
HO-7	LU+10	3.09	402	0.23	d_h-->d_e
HO-8	LU+6	2.97	417	0.23	p_h-->p_e

Table 1: Table showing the 10 most intense optical transitions between states HO-x and LU+y based on oscillator strength f_{ij} with corresponding transition energy E_{trans}. Each transition is also categorized by the envelope function symmetry of the respective HO-x and LU+y state. It is seen that four of the top five most intense transitions are of $s_h \rightarrow s_e$ character.

HO-x	LU+y	$<f_{ij}>$	k_{rad} [1/ns]	$k_{non-rad}$ [1/ns]	PLQY
HO	LU	0.32	1.01	0.85	53%
HO	LU+1	0.30	0.95	0.73	
HO-1	LU	0.30	0.94	1.01	
HO-1	LU+1	0.29	0.92	0.76	

Table 2: Table showing the four possible radiative and non-radiative transitions in our two state (twice degenerate) model. $<f_{ij}>$ represents the time averaged oscillator strength between state HO-x and LU+y and is used to compute k_{rad} through the Einstein coefficient for spontaneous emission. $k_{non-rad}$ is found from Redfield tensor elements, where k_{rad} and $k_{non-rad}$ determine PLQY.

TOC Graphic

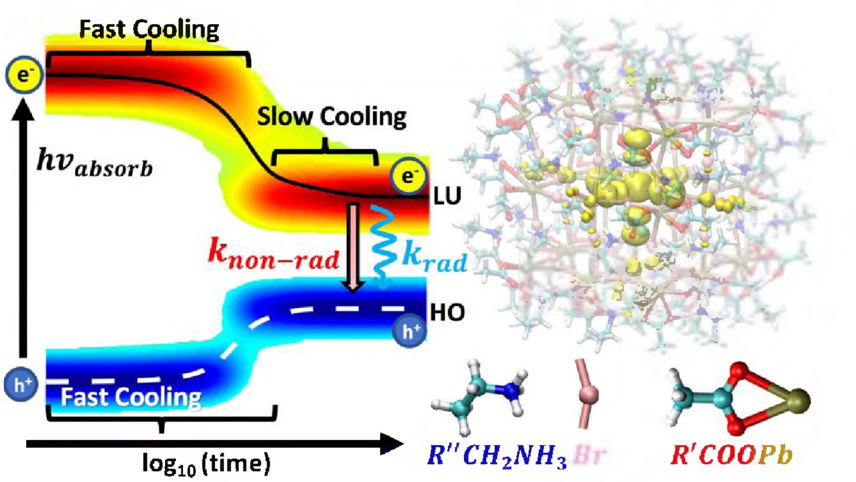
Fast Cooling
e⁻
Slow Cooling
hv_{absorb}
e⁻
LU
$k_{non-rad}$
k_{rad}
HO
h⁺
h⁺
Fast Cooling
log₁₀ (time)
$R''CH_2NH_3$
Br
$R'COOPb$